Long-distance SLAM scanning of mine tunnel - testing of precision and accuracy of Emesent Hovermap ST-X

Tomáš KŘEMEN[1]*, Ondřej MICHAL[2], Tomáš JIŘIKOVSKÝ[3] and Ivan KURIC[4]

Authors' affiliations and addresses:

[1] Department of Special Geodesy, Faculty of Civil Engineering, Czech Technical University in Prague, Thákurova 7, 166 36 Prague 6, Czech Republic
e-mail: tomas.kremen@fsv.cvut.cz

[2] Department of Special Geodesy, Faculty of Civil Engineering, Czech Technical University in Prague, Thákurova 7, 166 36 Prague 6, Czech Republic
e-mail: ondrej.michal@fsv.cvut.cz

[3] Department of Special Geodesy, Faculty of Civil Engineering, Czech Technical University in Prague, Thákurova 7, 166 36 Prague 6, Czech Republic
e-mail: tomas.jirikovsky@fsv.cvut.cz

[4] Faculty of Mechanical Engineering and Computer Science, University of Bielsko-Biala, ul. Willowa 2, 43-309 Bielsko-Biala, Poland
e-mail: kuric.ivan@gmail.com

*Correspondence:
Tomáš Křemen, Department of Special Geodesy, Faculty of Civil Engineering, Czech Technical University in Prague, Thákurova 7, 166 36 Prague 6, Czech Republic
tel.: +420-22435-4668
e-mail: tomas.kremen@fsv.cvut.cz

Abstract

This paper presents a detailed analysis of the Emesent Hovermap ST-X LiDAR scanner's precision in long-distance scanning of underground environments, specifically within the Josef mine's main gallery. The experiment aimed to evaluate the simultaneous localization and mapping (SLAM) capabilities of the Hovermap ST-X over a 750-meter straight tunnel section where conventional geodetic reference points are unavailable. To validate the scanner's accuracy, reference measurements were obtained using a Leica ScanStation P40 terrestrial laser scanner and a Leica MS60 total station, establishing a millimeter-level geodetic network with spherical control targets. The SLAM-based Hovermap ST-X scanner captured point clouds in both single (1P) and double (2P) pass modes, which were then analyzed for systematic errors in transverse (X), longitudinal (Y), and vertical (Z) directions using RMSE metrics. The study finds that while the Hovermap ST-X provides high-precision point clouds within shorter sections, cumulative errors arise over the entire 750-meter distance, particularly in the longitudinal axis, leading to slight compressions that necessitate scale corrections. In the transverse direction, the deviations reach up to tens of centimetres. The study also highlights that double-pass scans effectively reduce transverse deviation errors compared to single-pass measurements, yet significant systematic errors persist in both vertical and horizontal planes. These findings suggest that while SLAM scanning offers rapid data acquisition and adequate accuracy for various applications, its precision for geodetic surveys over extended distances could be improved by integrating scaling transformations and optimized pathing strategies. This work demonstrates the SLAM scanner's utility in challenging underground conditions and provides a framework for future precision assessments in mine surveying. The results suggest practical considerations for enhancing SLAM-based mapping accuracy in geodetic applications, emphasizing the need for periodic control points to minimize cumulative drift errors.

Keywords

SLAM, 3d scanning, underground, mine, precise measurement, accuracy testing

Introduction

3D scanning is currently used to capture reality in a wide range of fields. For precision measurements where spatial positioning accuracy in the sub-unit centimetre range is required, static terrestrial scanning systems with nominal accuracy in millimetres are used (Adhikari et al., 2023), (Urban et al., 2019), (Kovanič et al., 2020b). For large-scale mapping work where lower accuracy is required, ground mobile scanning systems (Di Stefano et al., 2021), (Kalvoda et al., 2020) mounted on cars or similar vehicles and airborne scanning systems (lidars) mounted on unmanned aerial vehicles (UAVs) are used (Kovanič et al., 2023), (Park & Choi, 2020), (Štroner et al., 2021a), (Kovanič et al., 2020a). Currently, digital photogrammetry is also very often used in connection with UAVs for mapping large areas (Losè et al., 2021), (Teo et al., 2023), (Štroner et al., 2021b), (Nesbit et al., 2022), (Kovanič et al., 2021a), (Kovanič et al., 2021b), (Cirillo et al., 2022), (Kovanič et al., 2024).

The advantages of 3D scanning include the complete capture of the area of interest with a large number of detailed points in a very short time at a high level of detail. The result of the measurement is a so-called point cloud. This can be further processed into various forms of output, such as CAD models or digital terrain models (Kovanič et al., 2023) . The resulting outputs can be used in a wide range of fields: as-built documentation, mapping (Běloch and Pavelka, 2024), cultural heritage, building information modelling (BIM), forestry, agriculture and last but not least in underground spaces (Pukanská et al., 2023), (Pinpin et al., 2021), (Giordan et al., 2021), (Pukanská et al., 2020). As can be seen from many articles, post-processing of point clouds is also very important. Ground detection (filtering vegetation) or reduction of noise (Štular & Lozić, 2020), (Štroner et al., 2022), (Tomková et al., 2022), (Wang & Koo, 2021), (Hui et al., 2021) are usually used, whereas in recent years also with the use of neural networks (Baiocchi et al., 2023), (Štroner et al., 2023).

Among the latest technologies used in the field of 3D scanning are handheld scanning systems based on the simultaneous localization and mapping (SLAM) algorithm (Akpinar, 2021). Their great advantage is the very fast acquisition of complex spaces, especially in building interiors and other enclosed areas (Chen et al., 2022), (Keitaanniemi et al., 2021), but it also works outdoors on bridge structures (Urban et al., 2024), (Previtali et al., 2020). SLAM systems are carried by an operator walking at a leisurely pace through the space of interest, where after passing through it (usually moving forth and back or in loops, with the latest devices, only a pass forth is sufficient), a point cloud of the location of interest is generated in a local coordinate system. However, this generated cloud is without any control, which can be considered as a disadvantage of this technology. The main errors that can occur can be divided into the overall failure of the SLAM algorithm and the measurement errors of the system itself.

The above-mentioned shortcomings of this technology are being addressed by its continuous development (Kopáčik et al., 2022), (Li et al., 2023), (Li et al., 2024), (Kovanič et al., 2021) and testing. In the field of underground spaces, it has been tested in (Singh et al., 2023), (Fasiolo et al., 2023), (Wajs et al., 2018).

Further extensive testing of SLAM scanners in the underground area, specifically in the mine, was also performed in the paper (Štroner et al., 2024). Here, a comprehensive procedure for testing SLAM scanners in underground spaces was described, including the acquisition of individual sub-error components on the highly uneven surface of mine tunnels. Testing was carried out in a corridor approximately 100 m long. Of the results obtained, the Emesent Hoovermap ST-X scanning system appeared to be the most accurate (10 mm accuracy achieved).

Therefore, a new experiment was designed to verify the performance of the Emesent Hoovermap ST-X scanning system in a much longer mine corridor (750 m), the results of which are presented in this paper.

Materials and methods

The experiment was carried out in the environment of a mine with walls formed by irregular rough stones. The geodetic network was created with a Leica MS60 total station with millimetre accuracy in the tested area. The reference point cloud was measured by static terrestrial laser scanner Leica ScanStation P40 in seven profiles. Six spherical targets (diameter 0.145 m) were determined from the reference point cloud (three targets in the first and last profile). These targets were used only to transform the tested point clouds from the scanning system EmesentHovermap ST-X into the same coordinate system. The accuracy of the tested scanner was subsequently determined by comparing the point clouds in the profiles scanned by the reference scanner.

Experiment Area

The test was performed in the main gallery of the Josef mine, which is operated by the Josef Regional Underground Research Centre (URC Josef) of the Czech Technical University in Prague, Faculty of Civil Engineering (https://ceg.fsv.cvut.cz/). The area is approx. 750 m long straight tunnel. The tunnel is, on average, 3.5 m wide and 3 m high, see Fig. 1 b). The black part of the main gallery was used for the experiment, highlighted green parts were compared profiles, see Fig. 1 c); blue dots were black and white targets serving as ground control

points (GCP) for the transformation of P40 scans and red dots were GCP spherical targets, see Fig. 1 a). The GCP coordinate system was designed with the X-axis perpendicular to the tunnel, the Y-axis longitudinal to the tunnel, and the Z-axis oriented upwards.
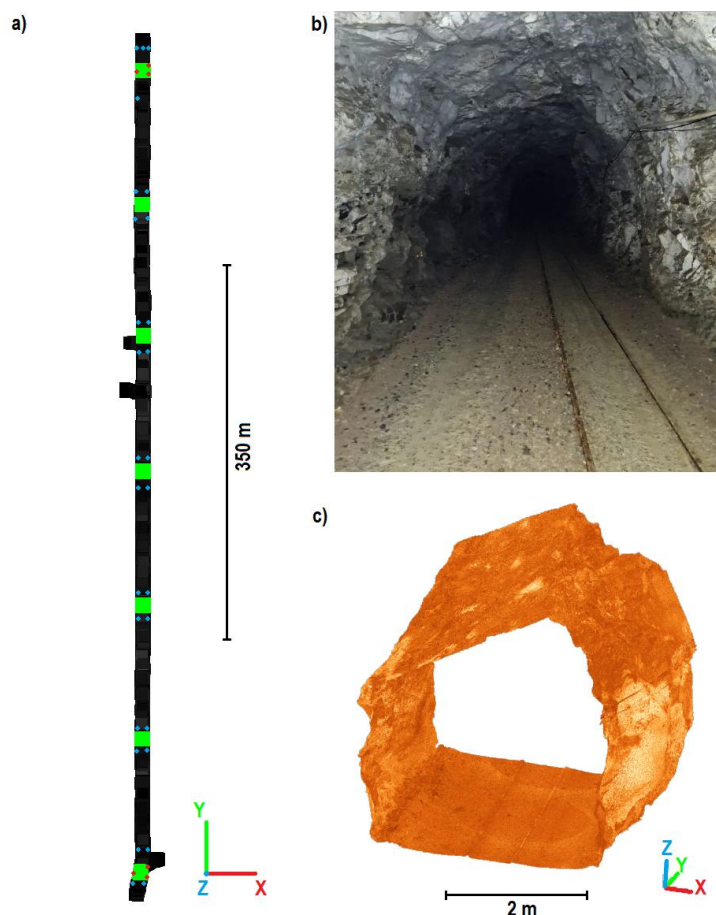

Fig. 1. a) the experiment area – the profiles are highlighted in green, the spherical targets are highlighted in blue and black and white targets are highlighted in red; b) photo of the main gallery tunnel; c) 3D view of the tunnel profile.

The used devices and software

The Leica Nova MS60 robotic total station (Leica Geosystems AG, Switzerland), Fig. 2 a), has a standard deviation of distance measurement of 1.0 mm + 1.5 ppm for the prism and 2 mm + 2 ppm for any arbitrary surface and a standard deviation of horizontal direction and zenith angle measurement 0.3 mgon. It was used to measure the geodetic network.

The Leica ScanStation P40 terrestrial scanner (Leica Geosystems AG, Switzerland), Fig. 2 b), has a standard deviation of distance measurement of 1.2 mm + 10 ppm and a standard deviation of the horizontal direction and zenith angle measurement of 2.4 mgon. The range of the measured distance is from 0.4 m to 270 m at a reflectance of 34%. The field of view is 360° × 270°, and the scanning rate is up to 1 million points per second. It is equipped with a liquid compensator with an accuracy of 0.45 mgon. The scanner was used to scan reference point clouds. Black and white targets were used to georeference each point cloud. The centres of the targets were acquired by a special scanning procedure. These targets were georeferenced with a Leica MS60 total station. The data were processed using the Leica Cyclone software.

The Emesent Hovermap ST-X (Emesent Pty Ltd., Australia), Fig. 2 c) is a SLAM scanner. It has a LiDAR precision of 10 mm and a mapping accuracy of 15 mm in general environments, 10 mm in indoor and underground environments and a local accuracy of 5 mm. The LiDAR has 32 channels. The range of measured distance is from 0.5 m to 300 m. The field of view is 290°x360°, and the scanning rate is up to 640000 points per second (single return mode) or up to 1.92 million points per second (multi return mode, 3 returns). The weight of the scanner is 1.57 kg. It can be handheld or mounted on a backpack (this experiment) or any other vehicle (ground vehicle, unmanned aerial vehicle, ground robot). Data were processed using the Emesent Aura software.
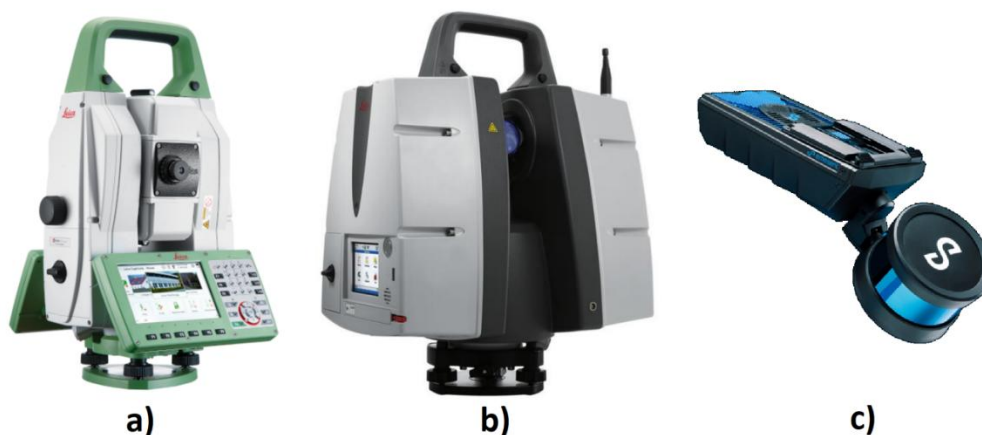
Fig. 2. a) the Leica Nova MS60 robotic total station; b) the Leica ScanStation P40; c) the Emesent Hovermap ST-X

Measurement and processing of the reference dataset

First, the geodetic network was surveyed with a Leica MS60 total station that, according to testing (Braun et al., 2015), (Vaněček & Štroner, 2016), achieves a very small systematic error. The measurements were carried out in two groups and from three stations. The geodetic network was adjusted as a free network using the least squares method with 83 redundant measurements. The coordinates of the points in the geodetic network were determined with an expected accuracy of 1 mm. The adjustment of the network was performed using a robust algorithm that automatically detects outliers (Třasák & Štroner, 2014), (Štroner et al., 2014). Twenty-eight black-and-white targets were determined, which were equally placed in groups of four around all seven reference profiles.

The reference point clouds were measured with a Leica P40 scanning system. Three positions were measured at 2 m spacing on each of the seven reference profiles. The individual scans in the profile were joined to each other based on the ICP algorithm overlay area and georeferenced with black and white targets (four targets for each position). The mean absolute errors of these georeferencing were 1 mm or better. After georeferencing, spherical targets were modelled on the first and last profiles, which further served as GCP spherical targets for transforming the validated data. The measurement was processed in Leica Cyclone ver. 2023.0.1 software.

Measurement and processing with the Emesent Hovermap ST-X scanner

The evaluated scanner was tested based on tunnel scanning without any auxiliary georeferencing. For each measurement, the entire test area was scanned, with emphasis on locating the spherical targets placed three by three at the beginning and end of the area.

The measurements were performed according to the scanner manufacturer's recommended procedure. First, the area was scanned five times using a single path (1P), where the first one was measured forth, the second path was measured back (the operator walked the opposite direction), and so on. Then, the area was scanned five times using a double path (forth and back without interruption of measurement, 2P). A total of 10 measurements were taken. The one-way path took approximately 10 minutes, and the two-way path took approximately 20 minutes. The time includes turning on the scanner, initializing it, passing through the area and turning it off.

Basic processing of the data from the Emesent Hoovermap ST-X scanner was performed in Emesent Aura software using a common procedure used in practice. The obtained primary point cloud in the local coordinate system was then imported into CloudCompare ver. 2.13.2 software, where all subsequent steps required for the evaluation were performed.

The first step performed in the Cloucompare software was to transform the primary point clouds from the Emesent system into a reference coordinate system defined by six spherical GCP targets (blue dots, see Fig. 1a). The points representing the spherical GCP targets in the Emesent clouds were cut and carefully cleaned. The transformation parameters (three angles of rotation about the axes, three displacements in the direction of the axes and root mean square of transformation - RMSt) were obtained using the Align (point pairs picking) function in Tools/Registration, where the sphere centres were determined using the Pick spheres option. These parameters were used to transform the primary point clouds (custom parameters were specified for each cloud) into the reference coordinate system.

The transformation parameters for the congruence and similarity transformation were determined for each primary point cloud. A total of 20 point clouds were obtained from Emesent. In the next step, the parts of the clouds corresponding to the reference control profiles from the P40 system were cut out for each checked point cloud and the two transformation variants. The cut portions were trimmed and cleaned so that the reference point cloud overlapped at all points in the profile.

An evaluation of the quality of the point clouds was performed on the prepared data. The quality evaluation is based on the determination of the systematic shifts of the test clouds with respect to the reference clouds and the determination of the root mean square error (*RMSE*) between the test and reference clouds.

The systematic displacement of the controlled clouds relative to the reference clouds of each profile was calculated in two steps. First, the clouds were shifted so that the centre of gravity of the test cloud was located at the origin of the coordinate system. The same displacement was applied to the reference cloud to maintain their relative positions. This was done to avoid artefacts caused by rotating the cloud about a distant beginning of the coordinate system. To calculate the size of the shift, the move bounding box centre to origin function in Tools/Registration was used. Then, an ICP (Iterative closest point) transformation was performed using all points in the test cloud while enabling outliers to be removed. The fine registration (ICP) function in Tools/Registration was used. The obtained transformation parameters indicate the systematic shift in the respective directions ΔX, ΔY, and ΔZ are in Fig. 3.
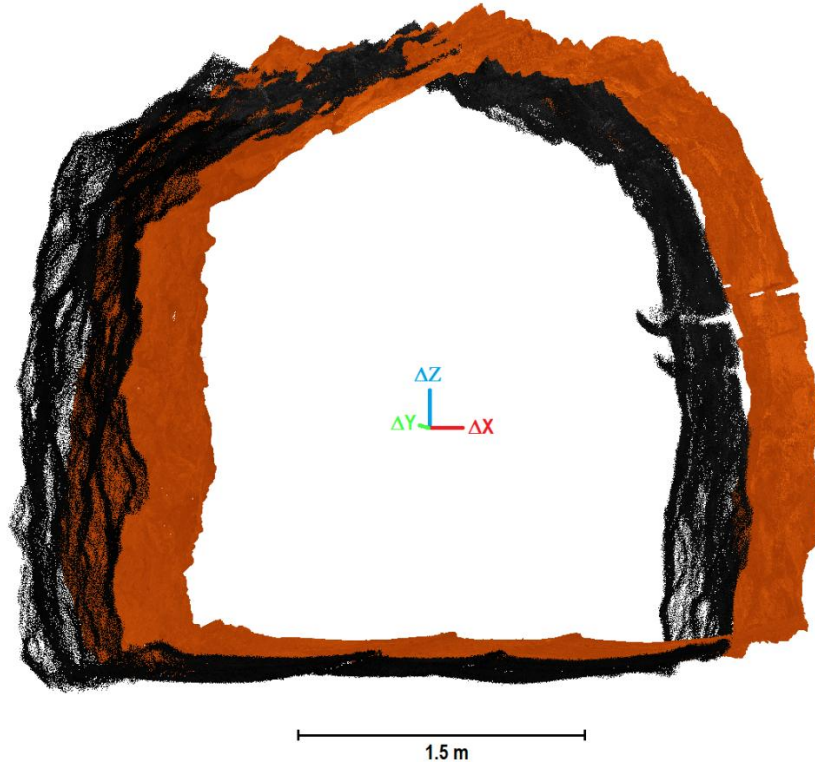
Fig. 3. Illustration of systematic shifts in transversal (ΔX), longitudinal (ΔY), and vertical (ΔZ) direction.

Local root mean square error (*RMSE_L*) (1) for each profile was calculated as:

$$RMSE_L = \sqrt{\frac{\sum_1^n d_i^2}{n}}, \tag{1}$$

where *n* is the number of points in the tested cloud and *d* is the smallest distance between the i_{th} point in the tested cloud and the surface defined by the reference cloud. The distances were obtained using the function "Compute cloud/cloud distance" in the tools/distances, which creates a local triangular irregular network (TIN) from the *k* nearest points (in our case, set to 15) from the reference cloud and determines the shortest distance between the ith point from the tested cloud and the reference local TIN.

Root mean square error (*RMSE_ΔX*) (2) was calculated from the systematic shifts ΔX for each profile. (*RMSE_ΔY*, *RMSE_ΔZ*) were calculated analogically.

$$RMSE_{\Delta X} = \sqrt{\frac{\sum_1^m \Delta X_j^2}{m}}, \tag{2}$$

where *m* is the number of repetitions of each type of measurement (1P and 2P), and *j* is the measurement index. From these, the mean errors in each axis (*Ø_RMSE*) (3) were then calculated as:

$$\emptyset_{RMSE_{\Delta X}} = \sqrt{\frac{\sum_1^u RMSE_{\Delta X_k}^2}{u}}, \tag{3}$$

where u is the number of profiles. In the other axes, it is calculated analogically again.

The last metric describing the distance of the test clouds is $RMSD_{OT}$ (4), which expresses the cumulative distance of the test clouds from the reference clouds in the transverse direction:

$$RMSD_{OT} = \sqrt{RMSE_{\Delta X}^2 + RMSE_{\Delta Z}^2}. \tag{4}$$

Results

For the *RMSE* transformation and the similarity transformation, the scale of the cloud transformation was recorded from the individual paths. These are shown in Tab. 1. In the table, we can see that the resulting *RMSE* transformation on spherical targets strongly depends on the type of transformation. For the congruence transformation, the $RMSE_{TI}$ is in the order of units of cm, while for the similarity transformation, it is an order of magnitude lower; the average $RMSE_{TS}$ of the multiple paths corresponds to the internal accuracy of the tested instrument. The scaling is greater than 1 for all paths, and the clouds from the instrument under test are smaller than they should be (on average by 10 cm per km).

Tab. 1. RMSE by transforming to unscaled and scaled reference points.

Measurement type	Path code	$RMSE_{TI}$	$RMSE_{TS}$	Scale
1P	1	44	4,9	1,00012
	2	29	9,1	1,00008
	3	38	7,3	1,00010
	4	27	7,5	1,00007
	5	32	5,2	1,00008
	$\emptyset_{1P}$	**34,6**	**7,0**	**1,00009**
2P	6	31	6,6	1,00008
	7	40	3,8	1,00011
	8	62	5,5	1,00017
	9	44	4,7	1,00011
	10	70	5,1	1,00018
	$\emptyset_{2P}$	**51,4**	**5,2**	**1,00013**

Transverse, longitudinal and height systematic shifts in individual profiles from all passes are given in the Appendix in Tab A.1 and Tab A.2 for reasons of scale. Here we present the aggregated results from multiple passes - five one-way and five two-way passes, each with scale 1 (S=1) and general (S≠1) (see Tab. 1). From the average shifts of $\emptyset_{RMSE}$, we can observe that in case of 1P, the highest shift is in the X-axis (perpendicular to the route), while in case of 2P the highest shift is in the vertical direction, which does not change depending on the number of passes. The harmonic mean was also calculated from the $RMSE_L$, which describes the local accuracy in the profiles. The $RMSE_L$ does not differ much between profiles and processing methods and corresponds to the local accuracy given by the manufacturer.

Tab. 2. Aggregated RMSE versus measurement type (1P x 2P) and processing method (S=1 x S≠1, where S denotes scale)

[mm]	profile	0	1	2	3	4	5	6	$\emptyset_{RMSE}$
1P S=1	$RMSE_{\Delta X}$	3,3	139,3	238,5	279,1	253,4	154,7	1,7	**186,1**
	$RMSE_{\Delta Y}$	29,4	29,0	18,5	11,3	19,4	24,1	29,9	**24,0**
	$RMSE_{\Delta Z}$	3,5	86,0	121,2	117,5	108,8	89,6	3,7	**89,3**
	$RMSE_L$	6,7	6,5	7,2	7,2	7,0	7,1	7,1	**7,0**
	$RMSD_{OT}$	**4,8**	**163,7**	**267,6**	**302,8**	**275,8**	**178,8**	**4,0**	**206,4**
1P S≠1	$RMSE_{\Delta X}$	3,7	140,0	239,2	279,2	253,7	154,5	2,8	**186,3**
	$RMSE_{\Delta Y}$	2,3	15,0	14,3	10,9	11,0	8,1	2,4	**10,3**
	$RMSE_{\Delta Z}$	2,0	85,5	121,9	118,6	110,5	90,4	4,5	**90,0**
	$RMSE_L$	6,6	6,4	7,1	7,2	7,0	6,9	6,8	**6,9**
	$RMSD_{OT}$	**4,2**	**164,0**	**268,5**	**303,3**	**276,7**	**179,0**	**5,3**	**206,9**

	$RMSE_{\Delta X}$	1,0	49,9	84,5	107,7	96,4	53,6	1,5	**69,1**
	$RMSE_{\Delta Y}$	44,1	32,7	18,1	4,4	20,8	30,4	44,4	**30,9**
2P S=1	$RMSE_{\Delta Z}$	1,4	88,2	122,4	117,0	115,3	100,2	4,8	**92,4**
	$RMSE_L$	6,9	6,3	7,2	7,1	6,9	7,2	7,0	**7,0**
	$RMSD_{OT}$	**1,7**	**101,3**	**148,7**	**159,1**	**150,3**	**113,6**	**5,0**	**115,4**
	$RMSE_{\Delta X}$	1,8	48,2	83,9	107,6	96,6	54,4	1,7	**68,9**
	$RMSE_{\Delta Y}$	3,0	5,7	6,0	4,3	5,9	4,4	2,6	**4,8**
2P S≠1	$RMSE_{\Delta Z}$	3,9	90,0	124,4	117,7	114,9	97,8	2,1	**92,8**
	$RMSE_L$	6,6	6,3	7,1	7,0	6,7	6,8	6,7	**6,7**
	$RMSD_{OT}$	**4,3**	**102,1**	**150,0**	**159,5**	**150,2**	**112,0**	**2,7**	**115,6**

In all cases, $RMSE_{\Delta X}$ and $RMSE_{\Delta Z}$ have extrema at the middle profile and decrease with decreasing distance from the GCP. $RMSE_{\Delta Y}$ behaves the opposite in the case of the congruence transformation, which is due to the properties of the transformation. Then, in the case of the similarity transform, the RMSE is negligibly small in the longitudinal direction relative to the others.

The detailed error bars in each profile can be seen in Fig. 4. Here, we can also see that the type of transformation has a negligible effect on the errors in the other axes (blue and green lines on the left and on the right are almost the same) (this is due to the significantly smaller dimensions in these axes, so the scaling is not affected).
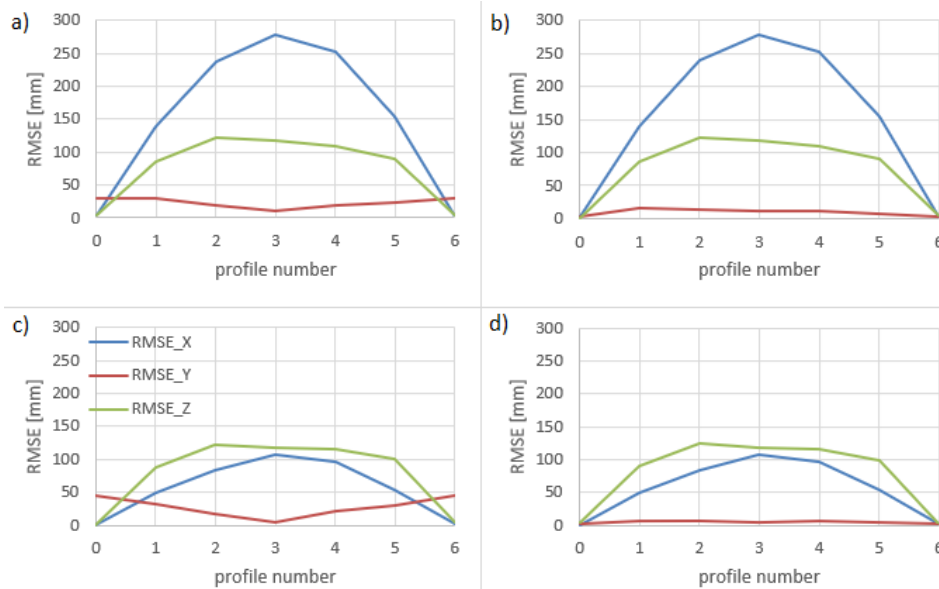

Fig. 4. Average transverse RMSE$_{\Delta X}$, longitudinal RMSE$_{\Delta Y}$ and elevation RMSE$_{\Delta Z}$ for each calculation variant a) 1P, S=1, b) 1P, S≠1, c) 2P, S=1, d) 2P, S≠1

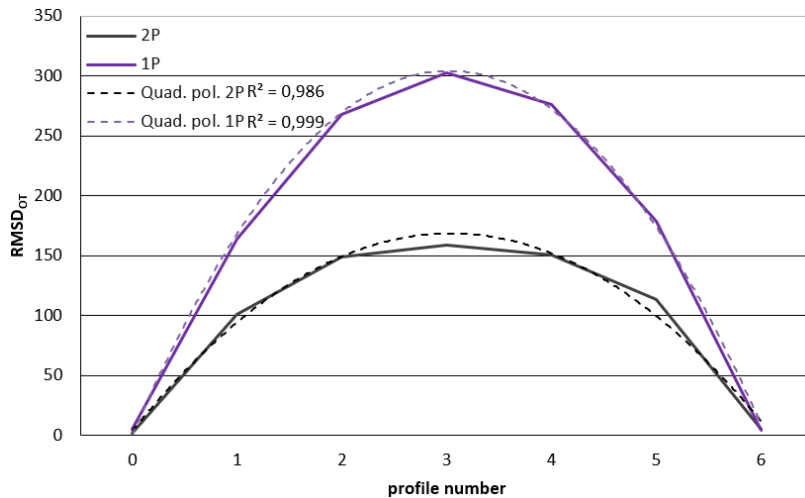
Fig. 5. Comparison of the total lateral deviation (RMSD$_{OT}$) for the 2P and 1P measurement variants in the profiles for S=1

In Fig. 5, we can see the pattern of the total lateral variation in the profiles for 1P and 2P. At 2P, the lateral distance of the clouds in the profiles is, on average, half that at 1P. Assuming that $RMSD_{OT}$ arises from the successive summation of measurement errors, these should have a quadratic pattern (the profiles were at regular intervals, so there is no need to consider distance). Therefore, the data were interleaved with a quadratic function (dashed line) that closely approximates the actual waveform, as confirmed by the calculated squared correlation coefficient, which is very close to 1 for both 1P and 2P.

From the average displacements, it is evident that the deviations within the cloud accumulate systematically, for ΔZ independent of the direction of travel and also independent of the number of passes, while for ΔX, the transverse shift direction changes with the direction of travel and decreases significantly when passing forth and back.

Tab. 3: Cumulative mean deviations depending on the type of measurement (1P x 2P) and processing method (S=1 x S≠1, where S denotes scale)

[mm]	profile	0	1	2	3	4	5	6	Ø
1P (forth) S=1	$\varnothing_{\Delta X}$	2,5	-100,1	-143,7	-139,8	-116,8	-85,5	-2,1	**-83,6**
	$\varnothing_{\Delta Y}$	-31,9	-18,2	-2,8	4,3	22,0	30,4	34,4	**5,5**
	$\varnothing_{\Delta Z}$	4,4	89,5	124,6	124,4	113,6	95,3	-1,3	**78,6**
	$\varnothing_{\Delta}$	**-8,4**	**-9,6**	**-7,3**	**-3,7**	**6,3**	**13,4**	**10,3**	**0,2**
1P (back) S=1	$\varnothing_{\Delta X}$	-4,0	172,4	315,2	390,1	364,5	217,1	0,3	**208,0**
	$\varnothing_{\Delta Y}$	-24,5	-39,0	-26,9	-12,4	7,8	8,0	20,9	**-9,4**
	$\varnothing_{\Delta Z}$	-0,8	78,4	111,4	103,6	95,8	76,7	4,5	**67,1**
	$\varnothing_{\Delta}$	**-9,8**	**70,6**	**133,3**	**160,4**	**156,1**	**100,6**	**8,6**	**88,5**
1P (forth) S≠1	$\varnothing_{\Delta X}$	0,3	-101,6	-144,6	-139,9	-115,3	-84,8	-3,0	**-84,1**
	$\varnothing_{\Delta Y}$	-1,3	0,6	5,6	2,4	10,0	7,7	-0,8	**3,5**
	$\varnothing_{\Delta Z}$	-0,3	87,7	124,7	125,6	115,9	96,2	1,4	**78,8**
	$\varnothing_{\Delta}$	**-0,4**	**-4,5**	**-4,8**	**-3,9**	**3,5**	**6,4**	**-0,8**	**-0,6**
1P (back) S≠1	$\varnothing_{\Delta X}$	-4,4	171,8	315,3	389,9	364,9	217,1	0,1	**207,8**
	$\varnothing_{\Delta Y}$	-0,4	-23,1	-19,4	-13,2	-1,0	-7,9	-3,5	**-9,8**
	$\varnothing_{\Delta Z}$	1,7	79,7	112,8	104,3	96,0	76,4	3,6	**67,8**
	$\varnothing_{\Delta}$	**-1,1**	**76,1**	**136,2**	**160,3**	**153,3**	**95,2**	**0,1**	**88,6**
2P S=1	$\varnothing_{\Delta X}$	0,3	45,0	75,4	96,8	83,3	45,9	-0,9	**49,4**
	$\varnothing_{\Delta Y}$	-41,4	-31,8	-17,1	0,7	20,3	29,6	41,8	**0,3**
	$\varnothing_{\Delta Z}$	0,7	86,8	121,1	115,2	112,7	98,3	4,4	**77,0**
	$\varnothing_{\Delta}$	**-13,5**	**33,3**	**59,8**	**70,9**	**72,1**	**57,9**	**15,1**	**42,2**
2P S≠1	$\varnothing_{\Delta X}$	-1,6	43,0	74,6	96,7	83,4	47,1	-1,3	**48,9**
	$\varnothing_{\Delta Y}$	2,0	-5,3	-3,6	0,7	5,5	3,4	-2,3	**0,1**
	$\varnothing_{\Delta Z}$	3,3	88,6	123,1	116,0	112,5	96,0	1,8	**77,4**
	$\varnothing_{\Delta}$	**1,2**	**42,1**	**64,7**	**71,2**	**67,2**	**48,9**	**-0,6**	**42,1**

Conclusion

When measuring with SLAM scanners at longer distances, errors must gradually accumulate; therefore, accuracy decreases with distance from the reference points. This has been tested with multiple SLAM scanners (Štroner, 2025). The Emesent Hovermap ST-X scanner performed comparably to static scanners in this test at a distance of about 100 m, and no significant systematic errors were identified. Therefore, an experiment on a multiply larger scale was designed and described in this paper.

At a distance of about 750 m between the reference points, significant shifts already appeared in the resulting cloud with respect to the geodetic use of the tested instrument. Several observations emerge from the statistical processing of the measured data. At such a large distance, the error in the longitudinal direction is systematically manifested (the cloud from the tested instrument was always smaller in the longitudinal direction than the reference). For such distances, it is necessary to consider using a transformation with a scale that is different from one. By considering the scale, the deviations are roughly halved.

The local cloud accuracy matched that of the instrument tested. The average $RMSE_L$ from all tests is 7 mm, with fluctuations up to 1 mm. Thus, there are no local deformations regardless of the distance from the reference points.

The transverse and vertical directions shifts were in the order of hundreds of mm and were not eliminated even by passing the area forth and back. In the vertical direction, the double pass had a negligible effect, while in the transverse direction, the deviations are significantly reduced by the double pass but still exceed 100 mm. In view of this, measurements in only one direction cannot be recommended (transverse error up to 430 mm), and even when passing forth and back, not all deviations are sufficiently reduced.

The transverse and vertical direction shifts are significantly systematic, yet their progression with increasing distance from the reference points corresponds to the theoretically assumed quadratic function. The systematic nature of the errors (especially in the vertical direction) may be due, for example, to the inhomogeneity of the scanned surfaces on the floor and ceiling (smooth floor x growing rock), causing a systematic sagging of the resulting point cloud. This should be investigated further for verification.

It was also found that the sign of the lateral error in single path measurements was dependent on the walking direction. For the measurement direction forth (northward direction), the cloud was bent to the other side than for the measurement direction back (southward direction). There is obviously some systematic effect present here that should be investigated further.

Thus, for the geodetic use of SLAM scanners in surveying larger areas, it is necessary to determine the ideal spacing of identical points that will reduce the magnitude of the deviations in the resulting cloud to an acceptable value while maintaining the high efficiency of SLAM scanners.

References

Adhikari, M. D., Kim, T., Yum, S., & Kim, J. (2023). Damage detection and monitoring of a concrete structure using 3D laser scanning. *Engineering Proceedings*. https://doi.org/10.3390/engproc2023036001.

Akpınar, B. (2021). Performance of Different SLAM Algorithms for Indoor and Outdoor Mapping Applications. *Applied System Innovation*, *4*(4), 101. https://doi.org/10.3390/asi4040101.

Baiocchi, A., Giagu, S., Napoli, C., Serra, M., Nardelli, P., & Valleriani, M. (2023). Artificial neural networks exploiting point cloud data for fragmented solid objects classification. *Machine Learning Science and Technology*, *4*(4), 045025. https://doi.org/10.1088/2632-2153/ad035e.

Běloch, L., & Pavelka, K. (2024). Optimizing Mobile Laser Scanning Accuracy for Urban Applications: A Comparison by Strategy of Different Measured Ground Points. *Applied Sciences*, *14*(8), 3387. https://doi.org/10.3390/app14083387.

Braun, J., Štroner, M., Urban, R., & Dvoček, F. (2015). Suppression of Systematic Errors of Electronic Distance Meters for Measurement of Short Distances. *Sensors*, *15*(8), 19264–19301. https://doi.org/10.3390/s150819264

Chen, W., Zhou, C., Shang, G., Wang, X., Li, Z., Xu, C., & Hu, K. (2022). SLAM Overview: From Single Sensor to Heterogeneous Fusion. *Remote Sensing*, *14*(23), 6033. https://doi.org/10.3390/rs14236033.

Cirillo, D., Cerritelli, F., Agostini, S., Bello, S., Lavecchia, G., & Brozzetti, F. (2022). Integrating Post-Processing Kinematic (PPK)–Structure-from-Motion (SfM) with Unmanned Aerial Vehicle (UAV) Photogrammetry and Digital Field Mapping for Structural Geological Analysis. *ISPRS International Journal of Geo-Information*, *11*(8), 437. https://doi.org/10.3390/ijgi11080437.

Di Stefano, F., Torresani, A., Farella, E. M., Pierdicca, R., Menna, F., & Remondino, F. (2021). 3D Surveying of Underground Built Heritage: Opportunities and Challenges of Mobile Technologies. *Sustainability*, *13*(23), 13289. https://doi.org/10.3390/su132313289.

emesent.com. (n.d.). Hovermap ST-X Extends the Reach of Autonomous LiDAR Mapping. *emesent.com*. Retrieved from https://emesent.com/wp-content/uploads/2022/11/Hovermap-ST-X-product-brochure.pdf (accessed 27 September 2024).

Fasiolo, D. T., Scalera, L., & Maset, E. (2023). Comparing LiDAR and IMU-based SLAM approaches for 3D robotic mapping. *Robotica*, *41*(9), 2588–2604. https://doi.org/10.1017/s026357472300053x.

Giordan, D., Godone, D., Baldo, M., Piras, M., Grasso, N., & Zerbetto, R. (2021). Survey Solutions for 3D Acquisition and Representation of Artificial and Natural Caves. *Applied Sciences*, *11*(14), 6482. https://doi.org/10.3390/app11146482.

Hui, Z., Jin, S., Xia, Y., Nie, Y., Xie, X., & Li, N. (2020). A mean shift segmentation morphological filter for airborne LiDAR DTM extraction under forest canopy. *Optics & Laser Technology*, *136*, 106728. https://doi.org/10.1016/j.optlastec.2020.106728.

Kalvoda, P., Nosek, J., Kuruc, M., Volarik, T., & Kalvodova, P. (2020). Accuracy Evaluation and Comparison of Mobile Laser Scanning and Mobile Photogrammetry Data. *IOP Conference Series Earth and Environmental Science*, *609*(1), 012091. https://doi.org/10.1088/1755-1315/609/1/012091.

Keitaanniemi, A., Virtanen, J., Rönnholm, P., Kukko, A., Rantanen, T., & Vaaja, M. (2021). The Combined Use of SLAM Laser Scanning and TLS for the 3D Indoor Mapping. *Buildings*, *11*(9), 386. https://doi.org/10.3390/buildings11090386.

Kopacik, A., Kajanek, P., Brindza, J., Erdelyi, J., & Kyrinovic, P. (2022). DEVELOPMENT OF A MOBILE MAPPING SYSTEM FOR SIMULTANEOUS LOCALIZATION AND MAPPING. *International Multidisciplinary Scientific GeoConference SGEM . . .* https://doi.org/10.5593/sgem2022/2.1/s09.24.

Kovanič, Ľ., Blistan, P., Štroner, M., Urban, R., & Blistanova, M. (2021). Suitability of Aerial Photogrammetry for Dump Documentation and Volume Determination in Large Areas. *Applied Sciences*, *11*(14), 6564. https://doi.org/10.3390/app11146564.

Kovanič, Ľ., Blistan, P., Urban, R., Štroner, M., Blišťanová, M., Bartoš, K., & Pukanská, K. (2020a). Analysis of the Suitability of High-Resolution DEM Obtained Using ALS and UAS (SfM) for the Identification of Changes and Monitoring the Development of Selected Geohazards in the Alpine Environment—A Case Study in High Tatras, Slovakia. *Remote Sensing*, *12*(23), 3901. https://doi.org/10.3390/rs12233901.

Kovanič, Ľ., Blistan, P., Urban, R., Štroner, M., Pukanská, K., Bartoš, K., & Palková, J. (2020b). Analytical Determination of Geometric Parameters of the Rotary Kiln by Novel Approach of TLS Point Cloud Segmentation. *Applied Sciences*, *10*(21), 7652. https://doi.org/10.3390/app10217652.

Kovanič, Ľ.; Ambriško, Ľ.; Marasová, D.; Blišťan, P.; Kasanický, T.; Cehlár, M. Long-Exposure RGB Photography with a Fixed Stand for the Measurement of a Trajectory of a Dynamic Impact Device in Real Scale. *Sensors* 2021, *21*, 6818. https://doi.org/10.3390/s21206818

Kovanič, Ľ.; Blistan, P.; Rozložník, M.; Szabó, G. UAS RTK/PPK photogrammetry as a tool for mapping the urbanized landscape, creating thematic maps, situation plans and DEM. Acta Montan. Slovaca 2021, 26, 649–660.

Kovanič, Ľ.; Štroner, M.; Urban, R.; Blišťan, P. Methodology and Results of Staged UAS Photogrammetric Rockslide Monitoring in the Alpine Terrain in High Tatras, Slovakia, after the Hydrological Event in 2022. *Land* 2023, *12*, 977. https://doi.org/10.3390/land12050977

Kovanič, Ľ., Štroner, M., Blistan, P., Urban, R., & Boczek, R. (2023). Combined ground-based and UAS SfM-MVS approach for determination of geometric parameters of the large-scale industrial facility – Case study. *Measurement*, *216*, 112994. https://doi.org/10.1016/j.measurement.2023.112994.

Kovanič, Ľ.; Peťovský, P.; Topitzer, B.; Blišťan, P. Complex Methodology for Spatial Documentation of Geomorphological Changes and Geohazards in the Alpine Environment. *Land* 2024, *13*, 112. https://doi.org/10.3390/land13010112

leica-geosystems.com. (n.d.). Leica Nova MS60 robotic total station datasheet. *leica-goesystems.com.* Retrieved from https://leica-geosystems.com/-/media/files/leicageosystems/products/datasheets/leica_nova_ms60_ds.pdf?sc_lang=en&hash=786EB1A585205F6CDF37FF43C316F005 (accesed 27 September 2024).

leica-geosystems.com. (n.d.). ScanStation P40 terrestrial scanner datasheet. *leica-goesystems.com.* Retrieved from https://leica-geosystems.com/-/media/files/leicageosystems/products/datasheets/leica_scanstation_p30-p40_civil_ds.pdf?sc_lang=en&hash=966549BA70CE8A5E7AA2E3029C75FEA5 (accesed 27 September 2024).

Li, J., Wu, W., Yang, B., Zou, X., Yang, Y., Zhao, X., & Dong, Z. (2023). WHU-Helmet: A Helmet-Based Multisensor SLAM Dataset for the Evaluation of Real-Time 3-D Mapping in Large-Scale GNSS-Denied Environments. *IEEE Transactions on Geoscience and Remote Sensing*, *61*, 1–16. https://doi.org/10.1109/tgrs.2023.3275307.

Li, J., Yuan, S., Cao, M., Nguyen, T., Cao, K., & Xie, L. (2024). HCTO: Optimality-aware LiDAR inertial odometry with hybrid continuous time optimization for compact wearable mapping system. *ISPRS Journal of Photogrammetry and Remote Sensing*, *211*, 228–243. https://doi.org/10.1016/j.isprsjprs.2024.04.004.

Losè, L. T., Chiabrando, F., & Tonolo, F. G. (2020). Boosting the Timeliness of UAV Large Scale Mapping. Direct Georeferencing Approaches: Operational Strategies and Best Practices. *ISPRS International Journal of Geo-Information*, *9*(10), 578. https://doi.org/10.3390/ijgi9100578.

Nesbit, P. R., Hubbard, S. M., & Hugenholtz, C. H. (2022). Direct Georeferencing UAV-SfM in High-Relief Topography: Accuracy Assessment and Alternative Ground Control Strategies along Steep Inaccessible Rock Slopes. *Remote Sensing*, *14*(3), 490. https://doi.org/10.3390/rs14030490.

Park, S., & Choi, Y. (2020). Applications of Unmanned Aerial Vehicles in Mining from Exploration to Reclamation: A Review. *Minerals*, *10*(8), 663. https://doi.org/10.3390/min10080663.

Pinpin, L., Wenge, Q., Yunjian, C., & Feng, L. (2021). Application of 3D Laser Scanning in Underground Station Cavity Clusters. *Advances in Civil Engineering*, *2021*(1). https://doi.org/10.1155/2021/8896363.

Previtali, M., Brumana, R., & Banfi, F. (2020). Existing infrastructure cost effective informative modelling with multisource sensed data: TLS, MMS and photogrammetry. *Applied Geomatics*, *14*(S1), 21–40. https://doi.org/10.1007/s12518-020-00326-3.

Pukanská, K.; Bartoš, K.; Bakoň, M.; Papčo, J.; Kubica, L.; Barlák, J.; Rovňák, M.; Kseňak, Ľ.; Zelenakova, M.; Savchyn, I.; et al. Multi-Sensor and Multi-Temporal Approach in Monitoring of Deformation Zone with Permanent Monitoring Solution and Management of Environmental Changes: A Case Study of Solotvyno Salt Mine, Ukraine. Frontiers in Earth Science 2023, 11, doi:10.3389/feart.2023.1167672.

Pukanská, K., Bartoš, K., Bella, P., Gašinec, J., Blistan, P., & Kovanič, Ľ. (2020). Surveying and High-Resolution Topography of the Ochtiná Aragonite Cave Based on TLS and Digital Photogrammetry. *Applied Sciences*, *10*(13), 4633. https://doi.org/10.3390/app10134633.

Singh, S. K., Banerjee, B. P., & Raval, S. (2022). A review of laser scanning for geological and geotechnical applications in underground mining. *International Journal of Mining Science and Technology*, *33*(2), 133–154. https://doi.org/10.1016/j.ijmst.2022.09.022

Štroner, M., Urban, R., Křemen, T., Braun, J., Michal, O., & Jiřikovský, T. (2024). Scanning the underground: Comparison of the accuracies of SLAM and static laser scanners in a mine tunnel. *Measurement*, 115875. https://doi.org/10.1016/j.measurement.2024.115875.

Štroner, M., Urban, R., & Línková, L. (2021a). A New Method for UAV Lidar Precision Testing Used for the Evaluation of an Affordable DJI ZENMUSE L1 Scanner. *Remote Sensing*, *13*(23), 4811. https://doi.org/10.3390/rs13234811.

Štroner, M., Urban, R., & Línková, L. (2022). Multidirectional Shift Rasterization (MDSR) Algorithm for Effective Identification of Ground in Dense Point Clouds. *Remote Sensing*, *14*(19), 4916. https://doi.org/10.3390/rs14194916.

Štroner, M., Urban, R., & Línková, L. (2023). Color-Based Point Cloud Classification Using a Novel Gaussian Mixed Modeling-Based Approach versus a Deep Neural Network. *Remote Sensing*, *16*(1), 115. https://doi.org/10.3390/rs16010115.

Štroner, M., Urban, R., Rys P. & Balek P. (2014). Prague Castle Area Local Stability Determination Assessment by the Robust Transformation Method. Acta Geodynamica Et Geomaterialia, 325–336. https://doi.org/10.13168/agg.2014.0020

Štroner, M., Urban, R., Seidl, J., Reindl, T., & Brouček, J. (2021b). Photogrammetry Using UAV-Mounted GNSS RTK: Georeferencing Strategies without GCPs. *Remote Sensing*, *13*(7), 1336. https://doi.org/10.3390/rs13071336.

Teo, T., Fu, Y., Li, K., Weng, M., & Yang, C. (2022). Comparison between image- and surface-derived displacement fields for landslide monitoring using an unmanned aerial vehicle. International Journal of Applied Earth Observation and Geoinformation, 116, 103164. https://doi.org/10.1016/j.jag.2022.103164

Štular, B., & Lozić, E. (2020). Comparison of Filters for Archaeology-Specific Ground Extraction from Airborne LiDAR Point Clouds. *Remote Sensing*, *12*(18), 3025. https://doi.org/10.3390/rs12183025.

Tomková, M., Potůčková, M., Lysák, J., Jančovič, M., Holman, L., & Vilímek, V. (2022). Improvements to airborne laser scanning data filtering in sandstone landscapes. *Geomorphology*, *414*, 108377. https://doi.org/10.1016/j.geomorph.2022.108377.

Třasák, P., & Štroner, M. (2014). Outlier detection efficiency in the high precision geodetic network adjustment. *Acta Geodaetica Et Geophysica*, *49*(2), 161–175. https://doi.org/10.1007/s40328-014-0045-9.

Urban, R., Štroner, M., Blistan, P., Kovanič, Ľ., Patera, M., Jacko, S., . . . Szabo, S. (2019). The Suitability of UAS for Mass Movement Monitoring Caused by Torrential Rainfall—A Study on the Talus Cones in the Alpine Terrain in High Tatras, Slovakia. *ISPRS International Journal of Geo-Information*, *8*(8), 317. https://doi.org/10.3390/ijgi8080317.

Urban, R., Štroner, M., Braun, J., Suk, T., Kovanič, Ľ., & Blistan, P. (2024). Determination of Accuracy and Usability of a SLAM Scanner GeoSLAM Zeb Horizon: A Bridge Structure Case Study. *Applied Sciences*, *14*(12), 5258. https://doi.org/10.3390/app14125258.

Vaněček, J., & Štroner, M. (2016). TESTING THE ACCURACY OF MEASURED VALUES IN CONTINUOUS LONG-TERM GEODETIC MONITORING. *Acta Polytechnica*, *56*(6), 478–491. https://doi.org/10.14311/ap.2016.56.0478.

Wajs, J., Kasza, D., Zagożdżon, P. P., & Zagożdżon, K. D. (2018). 3D modeling of underground objects with the use of SLAM technology on the example of historical mine in Ciechanowice (Ołowiane Range, The Sudetes). *E3S Web of Conferences*, *29*, 00024. https://doi.org/10.1051/e3sconf/20182900024.

Wang, Y., & Koo, K. (2021). Vegetation Removal on 3D Point Cloud Reconstruction of Cut-Slopes Using U-Net. *Applied Sciences*, *12*(1), 395. https://doi.org/10.3390/app12010395.

Appendix

Tab. A. 1: Transverse, longitudinal and height deviations in all profiles 1P, all in mm

path_1	forth	scale	1	[mm]				scale	1,00012	[mm]				
profile	0	1	2	3	4	5	6	0	1	2	3	4	5	6
ΔX	2,2	-34,3	-33,9	-20,0	-27,0	-42,4	-1,6	0,7	-35,0	-34,6	-20,1	-22,2	-41,5	-1,6
ΔY	-36,4	-28,3	-9,2	-2,7	8,6	27,9	38,8	2,0	-3,5	2,3	-2,9	-3,4	3,9	-0,7
ΔZ	5,3	82,6	118,0	121,1	128,7	114,1	1,4	2,3	80,4	117,9	122,5	131,3	118,3	7,3
RMSE$_L$	7,1	6,8	7,5	7,5	7,6	7,7	7,8	6,9	6,6	7,3	7,4	7,6	7,5	7,5
RMSD$_{OT}$	**5,7**	**89,4**	**122,8**	**122,7**	**131,5**	**121,7**	**2,1**	**2,4**	**87,7**	**122,9**	**124,1**	**133,2**	**125,4**	**7,5**
path_2	back	scale	1	[mm]				scale	1,000075	[mm]				
profile	0	1	2	3	4	5	6	0	1	2	3	4	5	6
ΔX	-2,5	159,4	278,1	350,1	331,5	198,6	0,7	-7,9	154,2	274,6	347,7	330,0	197,7	-0,8
ΔY	-28,9	-42,5	-32,8	-22,2	3,7	9,0	22,3	-1,9	-25,0	-24,3	-22,7	-5,2	-7,9	-3,4
ΔZ	-0,6	62,5	93,5	90,5	70,4	69,8	5,7	0,9	64,0	94,2	90,2	69,2	65,6	1,4
RMSE$_L$	6,4	6,5	7,3	7,3	6,9	7,2	6,7	6,3	6,4	7,2	7,2	6,8	7,0	6,5
RMSD$_{OT}$	**2,6**	**171,2**	**293,4**	**361,6**	**338,9**	**210,5**	**5,7**	**8,0**	**167,0**	**290,3**	**359,2**	**337,2**	**208,3**	**1,6**
path_3	forth	scale	1	[mm]				scale	1,0001	[mm]				
profile	0	1	2	3	4	5	6	0	1	2	3	4	5	6
ΔX	2,2	-113,9	-159,9	-169,1	-153,7	-103,7	-1,9	-1,1	-116,7	-160,7	-168,8	-153,3	-102,0	-1,8
ΔY	-31,6	-10,4	8,0	10,1	30,4	31,8	33,9	-2,8	6,0	14,8	6,7	16,6	7,5	-2,0
ΔZ	3,5	100,5	154,1	145,0	121,8	101,1	-4,5	-0,2	100,4	155,5	147,3	124,8	100,6	-3,2
RMSE$_L$	6,5	6,4	7,0	7,0	6,7	6,9	6,9	6,2	6,4	6,9	7,0	6,7	6,9	6,6
RMSD$_{OT}$	**4,1**	**151,9**	**222,0**	**222,8**	**196,1**	**144,8**	**4,9**	**1,1**	**153,9**	**223,6**	**224,0**	**197,6**	**143,3**	**3,7**
path_4	back	scale	1	[mm]				scale	1,00007	[mm]				
profile	0	1	2	3	4	5	6	0	1	2	3	4	5	6
ΔX	-5,4	185,4	352,3	430,1	397,6	235,6	0,0	-1,0	189,4	355,9	432,0	399,9	236,5	1,0
ΔY	-20,1	-35,4	-20,9	-2,7	11,9	6,9	19,6	1,1	-21,3	-14,5	-3,7	3,2	-7,9	-3,5
ΔZ	-1,1	94,2	129,3	116,8	121,3	83,7	3,4	2,4	95,5	131,4	118,5	122,8	87,1	5,9
RMSE$_L$	7,0	6,3	7,1	7,3	7,2	7,0	7,1	6,9	6,3	7,0	7,2	7,1	6,8	7,0
RMSD$_{OT}$	**5,5**	**208,0**	**375,3**	**445,6**	**415,7**	**250,0**	**3,4**	**2,6**	**212,1**	**379,4**	**447,9**	**418,3**	**252,0**	**5,9**
path_5	forth	scale	1	[mm]				scale	1,00008	[mm]				
profile	0	1	2	3	4	5	6	0	1	2	3	4	5	6
ΔX	3,1	-152,0	-237,4	-230,2	-169,6	-110,5	-2,9	1,4	-153,3	-238,5	-230,8	-170,3	-110,8	-5,7
ΔY	-27,7	-15,8	-7,2	5,3	27,0	31,6	30,4	-3,1	-0,7	-0,2	3,4	16,8	11,6	0,3
ΔZ	4,2	85,3	101,9	107,1	90,3	70,8	-0,7	-2,9	82,3	100,7	107,1	91,5	69,7	0,1
RMSE$_L$	6,7	6,4	7,0	6,9	6,6	6,5	6,8	6,5	6,4	7,0	6,9	6,6	6,5	6,6
RMSD$_{OT}$	**5,2**	**174,3**	**258,3**	**253,9**	**192,1**	**131,2**	**3,0**	**3,2**	**174,0**	**258,9**	**254,4**	**193,3**	**131,0**	**5,7**

Tab. A. 2: Transverse, longitudinal and height deviations in all profiles 2P, all in mm

path_6	Forth & back			scale	1	[mm]		scale	1,00008		[mm]			
profile	0	1	2	3	4	5	6	0	1	2	3	4	5	6
ΔX	-0,3	5,3	15,6	31,3	19,5	14,9	-1,3	-2,2	2,9	14,2	30,4	18,2	14,8	-3,3
ΔY	-22,1	-22,0	-12,0	0,7	16,1	22,2	22,9	4,8	-5,1	-2,8	1,1	7,9	7,7	-2,3
ΔZ	1,9	79,0	119,0	132,9	140,7	114,7	7,9	2,3	79,6	119,3	132,1	138,8	109,5	2,5
RMSE$_L$	6,7	6,4	7,3	6,9	6,8	7,4	7,1	6,6	6,3	7,2	6,8	6,7	7,0	6,9
RMSD$_{OT}$	**1,9**	**79,2**	**120,0**	**136,5**	**142,0**	**115,7**	**8,0**	**3,2**	**79,7**	**120,1**	**135,6**	**140,0**	**110,5**	**4,1**
path_7	Forth & back			scale	1	[mm]		scale	1,00011		[mm]			
profile	0	1	2	3	4	5	6	0	1	2	3	4	5	6
ΔX	0,1	44,7	57,2	62,4	43,1	19,2	-1,2	-2,4	42,3	56,5	62,9	43,3	21,3	-1,3
ΔY	-33,6	-28,8	-14,7	-4,6	14,3	23,1	32,5	1,7	-6,4	-3,2	-4,2	2,4	2,5	-2,4
ΔZ	1,0	98,8	124,8	110,9	100,6	75,6	4,9	6,0	103,7	129,4	113,6	101,6	72,1	0,9
RMSE$_L$	7,9	6,7	7,6	7,7	7,4	7,6	7,6	7,7	6,7	7,4	7,6	7,3	7,2	7,3
RMSD$_{OT}$	**1,0**	**108,4**	**137,3**	**127,3**	**109,4**	**78,0**	**5,0**	**6,5**	**112,0**	**141,2**	**129,9**	**110,4**	**75,2**	**1,6**
path_8	Forth & back			scale	1	[mm]		scale	1,00017		[mm]			
profile	0	1	2	3	4	5	6	0	1	2	3	4	5	6
ΔX	1,9	59,1	89,0	117,6	112,4	60,5	-0,8	-1,1	56,1	87,8	117,3	112,5	62,0	-0,8
ΔY	-54,7	-36,3	-14,2	3,7	23,4	32,2	55,5	3,4	-1,3	4,4	5,2	5,9	-0,3	-0,5
ΔZ	-0,5	88,2	128,3	122,0	116,4	105,1	2,4	2,4	90,2	131,2	123,9	117,5	104,4	1,5
RMSE$_L$	6,2	5,9	6,9	6,6	6,5	6,8	6,5	5,8	5,9	6,7	6,5	6,3	6,3	6,1
RMSD$_{OT}$	**2,0**	**106,2**	**156,1**	**169,5**	**161,8**	**121,3**	**2,5**	**2,6**	**106,2**	**157,9**	**170,6**	**162,7**	**121,4**	**1,7**
path_9	Forth & back			scale	1	[mm]		scale	1,00011		[mm]			
profile	0	1	2	3	4	5	6	0	1	2	3	4	5	6
ΔX	-1,0	69,2	131,0	168,8	156,0	89,6	1,2	-2,0	67,6	130,2	167,7	155,4	89,0	-0,6
ΔY	-33,8	-28,1	-16,3	7,1	22,1	29,5	35,1	2,0	-7,2	-6,3	5,4	7,7	5,2	-4,5
ΔZ	1,9	62,3	89,6	77,1	72,7	74,9	3,2	5,4	63,9	91,8	78,5	73,4	75,7	3,5
RMSE$_L$	6,9	6,7	7,6	7,7	7,3	7,6	7,2	6,7	6,7	7,5	7,6	7,1	7,1	7,0
RMSD$_{OT}$	**2,1**	**93,1**	**158,7**	**185,6**	**172,1**	**116,8**	**3,4**	**5,8**	**93,0**	**159,3**	**185,2**	**171,9**	**116,8**	**3,6**
path_10	Forth & back			scale	1	[mm]		scale	1,00018		[mm]			
profile	0	1	2	3	4	5	6	0	1	2	3	4	5	6
ΔX	0,8	46,5	84,1	104,1	85,4	45,4	-2,4	-0,3	46,0	84,3	105,4	87,6	48,6	-0,5
ΔY	-62,9	-43,8	-28,5	-3,3	25,7	41,0	63,1	-1,8	-6,7	-10,2	-4,1	3,8	1,8	-1,6
ΔZ	-1,0	105,8	143,7	132,9	133,0	121,0	3,8	0,3	105,7	143,9	132,1	131,4	118,5	0,7
RMSE$_L$	6,5	5,9	6,7	6,6	6,5	6,7	6,5	6,1	5,7	6,5	6,5	6,3	6,2	6,2
RMSD$_{OT}$	**1,3**	**115,6**	**166,5**	**168,8**	**158,1**	**129,2**	**4,5**	**0,5**	**115,3**	**166,8**	**169,0**	**157,9**	**128,1**	**0,9**